Prediction of texture-induced plastic anisotropy in AA6014-T4 aluminium sheets utilising two different crystal plasticity-based constitutive models

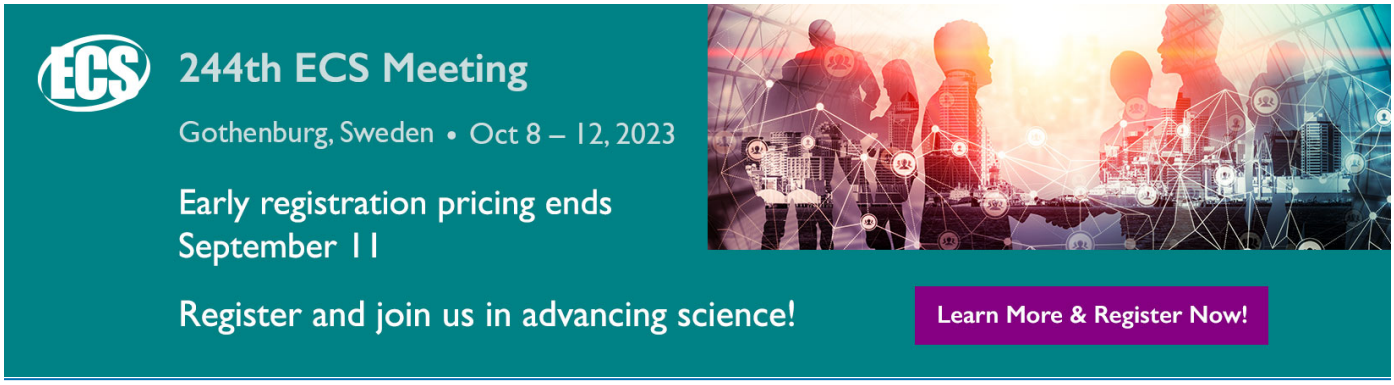

Prediction of texture-induced plastic anisotropy in AA6014-T4 aluminium sheets utilising two different crystal plasticity-based constitutive models

A Wessel[1,2], E S Perdahcıoğlu[3], A Butz[1], T van den Boogaard[3] and W Volk[2]

[1] Fraunhofer Institute for Mechanics of Materials IWM, Woehlerstrasse 11, 79108 Freiburg, Germany
[2] Chair of Metal Forming and Casting, Technical University of Munich, Walther-Meissner-Strasse 4, 85748 Garching, Germany
[3] Chair of Nonlinear Solid Mechanics, Faculty of Engineering Technology, University of Twente, Drienerlolaan 5, 7522 NB Enschede, The Nederlands

E-mail: alexander.wessel@iwm.fraunhofer.de

Abstract. Two crystal plasticity-based constitutive models that differ with respect to the flow rule (rate-dependent/rate-independent) and hardening law (phenomenological/physical-based), among other aspects, are compared with each other. To this end, both crystal plasticity-based constitutive models were deployed within a finite element framework to predict the texture-induced plastic anisotropy of an AA6014-T4 aluminium alloy considering uniaxial loading at 0°, 15°, 30°, 45°, 60°, 75° and 90° with respect to the rolling direction. The results of the stress-strain curves, the normalised yield stresses and the r-values demonstrate that both crystal plasticity-based constitutive models provide comparable results. Also, the experimental r-values were predicted with reasonable accuracy. Differences with respect to the experimental normalised yield stresses are discussed and were most likely caused by an additional direction-dependent mechanism.

1. Introduction

Information on plastic anisotropy in sheet metals is important for manufacturing sheet metal parts and for designing the necessary forming operations by using finite element simulations in particular. This plastic anisotropy is primarily caused by a preferred crystallographic texture, which develops during the rolling process of the sheet metal. To characterise plastic anisotropy of sheet metals, various experiments, such as uniaxial tensile tests in different directions, hydraulic bulge tests or plane strain tension tests, are typically applied [1, 2]. An alternative approach to analyse the plastic anisotropy of sheet metals are virtual experiments. Virtual experiments, or rather crystal plasticity simulations, utilise a crystal plasticity-based constitutive model to predict the plastic anisotropy based on the crystallographic texture. Thus, loading conditions that cannot be realised experimentally can be studied. For instance, Barlat et al. [3] performed virtual experiments on AA2090-T3 and AA6111-T4 aluminium sheets to characterise the plastic anisotropy regarding shear with respect to the thickness direction. In addition, there are many more examples in the literature [4-6], where virtual experiments were utilised to analyse the plastic anisotropy of sheet metals. However, most of these studies use slightly dissimilar crystal plasticity-based constitutive models that differ with respect to their mathematical formulation as well as their numerical implementation.

This study analyses the effect of two crystal plasticity-based constitutive models that differ with respect to the flow rule (rate-dependent/rate-independent) and hardening law (phenomenological/physical-based), among other aspects. To this end, both formulations are deployed to predict the texture-induced plastic anisotropy of an AA6014-T4 aluminium sheet. The results are compared with experimentally determined uniaxial tensile test in different directions with respect to the rolling direction (RD).

2. Material characterisation

2.1. Electron backscatter diffraction

AA6014-T4 aluminium sheets (Trademark Advanz™ 6F - e170) with a thickness of 1.0 mm were supplied by Novelis Switzerland SA. The crystallographic texture of these aluminium sheets was characterised by an electron backscatter diffraction (EBSD) measurement of the longitudinal cross-section. The EBSD measurement was conducted in a Zeiss Sigma 300 scanning electron microscope (SEM) equipped with an EBSD system by EDAX using APEX™ for data recording and OIM Analysis™ 8.6 for data processing. An area of roughly 2.5 mm x 0.9 mm using a hexagonal grid with a step size of 3.0 µm was scanned with an accelerating voltage of 20 kV. The EBSD data was analysed using the MATLAB toolbox MTEX 5.7.0 [7]. Only measurement points with a confidence index greater than 0.1 were considered for post-processing, as recommended by Field [8].

2.2. Uniaxial tensile tests

The mechanical material behaviour of AA6014-T4 was characterised by uniaxial tensile tests at 0°, 15°, 30°, 45°, 60°, 75° and 90° with respect to RD. Uniaxial tensile tests were performed on a ZwickRoell Kappa 50 DS uniaxial testing machine. The specimens were manufactured by water jet cutting and had a gauge length of 80 mm and gauge width of 20 mm in accordance with DIN EN ISO 6892-1, test piece type 2. All tensile tests were carried out until fracture using a constant engineering strain rate of 0.002 1/s. During the experiment, the change in the gauge length was measured in the longitudinal and transverse directions of the specimen using two tactile extensometers with accuracy class 0.5 according to EN ISO 9513. Three identical samples were tested for each direction. All uniaxial tensile tests were carried out two to three months after their final heat treatment at Novelis Switzerland SA.

3. Crystal plasticity modelling

3.1. Crystal plasticity-based constitutive models

The crystal plasticity-based constitutive models utilised in this study were available as UMAT user subroutines for the commercial finite element software Abaqus/Standard 2021. The first crystal plasticity-based constitutive model is based on the numerical framework presented in Kalidindi et al. [9] and is fully described in Pagenkopf [10]. A detailed summary of the second crystal plasticity-based constitutive model is given in Aşık et al. [11]. Hence, the following section focuses on the common fundamental equations of both formulations and their differences with respect to the flow rule (rate-dependent/rate-independent) and hardening law (phenomenological/physical-based).

The basis of both crystal plasticity-based constitutive models is the multiplicative decomposition of the deformation gradient into an elastic and plastic part:

$$\mathbf{F} = \mathbf{F}_\mathrm{e}\mathbf{F}_\mathrm{p}. \tag{1}$$

While the elastic part of the deformation gradient $\mathbf{F}_\mathrm{e}$ describes the reversible stretching and rotation of the crystal lattice, the plastic part of the deformation gradient $\mathbf{F}_\mathrm{p}$ defines the irreversible deformation due to crystallographic slip. Due to the multiplicative decomposition of the deformation gradient, the following applies to the velocity gradient:

$$\mathbf{L} = \dot{\mathbf{F}}\mathbf{F}^{-1} = \left(\dot{\mathbf{F}}_\mathrm{e}\mathbf{F}_\mathrm{p} + \mathbf{F}_\mathrm{e}\dot{\mathbf{F}}_\mathrm{p}\right)\mathbf{F}_\mathrm{p}^{-1}\mathbf{F}_\mathrm{e}^{-1} = \mathbf{L}_\mathrm{e} + \mathbf{F}_\mathrm{e}\mathbf{L}_\mathrm{p}\mathbf{F}_\mathrm{e}^{-1}. \tag{2}$$

The plastic part of the velocity gradient $\mathbf{L}_\mathrm{p}$ is defined as the sum of the shear rates $\dot{\gamma}$ acting on every slip system α:

$$\mathbf{L}_\mathrm{p} = \sum_{\alpha=1}^{n} \dot{\gamma}^{\alpha}\, \mathbf{m}^{\alpha} \otimes \mathbf{n}^{\alpha}. \tag{3}$$

The unit vectors $\mathbf{m}^{\alpha}$ and $\mathbf{n}^{\alpha}$ are the slip direction and the slip plane normal of the slip system, respectively. For face-centred cubic materials 12 slip systems, crystallographically called $\{111\}\ \langle 110\rangle$, are considered in both crystal plasticity-based constitutive models.

3.1.1. Flow rule. With respect to the flow rule, the first crystal plasticity-based constitutive model utilises a rate-dependent approach. To this end, the plastic shear rate $\dot{\gamma}$ is derived by

$$\dot{\gamma}^{\alpha} = \dot{\gamma}_0 \left|\frac{\tau^{\alpha}}{\tau_\mathrm{c}^{\alpha}}\right|^{1/m} \mathrm{sign}(\tau^{\alpha}) \tag{4}$$

as a power law-type equation, where $\dot{\gamma}_0$ and m are the reference shear rate and the rate sensitivity of slip, respectively. The resolved shear stress is calculated by Schmid's law

$$\tau^{\alpha} = (\mathbf{C}_\mathrm{e}\mathbf{S}) : (\mathbf{m}^{\alpha} \otimes \mathbf{n}^{\alpha}) \tag{5}$$

with

$$\mathbf{C}_\mathrm{e} = \mathbf{F}_\mathrm{e}^{\mathrm{T}}\mathbf{F}_\mathrm{e}. \tag{6}$$

The term $\mathbf{C}_\mathrm{e}\mathbf{S}$ is also known as the Mandel stress tensor, with $\mathbf{S}$ denoting the stress tensor in the intermediate configuration. The slip direction $\mathbf{m}^{\alpha}$ and the slip plane normal $\mathbf{n}^{\alpha}$ of a slip system are defined in the intermediate configuration. In Equation (4), the critical resolved shear stress τ_c^{α} of a slip system α evolves according to a phenomenological hardening law, which is described in Section 3.1.2.

The second crystal plasticity-based constitutive model uses a rate-independent formulation of the flow rule. Thus, crystallographic slip only occurs when the resolved shear stress τ^{α} is equal to the slip resistance τ_f^{α}:

$$\phi^{\alpha} = \tau^{\alpha} - \tau_f^{\alpha} \leq 0. \tag{7}$$

Here, the resolved shear stress τ^{α} of a slip system α is defined on the base of the Cauchy stress tensor $\boldsymbol{\sigma}$ in the current configuration as

$$\tau^{\alpha} = \boldsymbol{\sigma} : (\tilde{\mathbf{m}}^{\alpha} \otimes \tilde{\mathbf{n}}^{\alpha}). \tag{8}$$

In contrast to Equation (5), the slip direction $\tilde{\mathbf{m}}^{\alpha}$ and the slip plane normal $\tilde{\mathbf{n}}^{\alpha}$ of a slip system are given in the current configuration.

3.1.2. Hardening law. The hardening law for the critical resolved shear stress τ_c^{α} in Equation (4) of the rate-dependent crystal plasticity-based constitutive model is described by a phenomenological approach. As defined in Lebensohn et al. [12], the hardening rate of the critical resolved shear stress $\dot{\tau}_c^{\alpha}$ is given by

$$\dot{\tau}_\mathrm{c}^{\alpha} = \frac{\mathrm{d}\bar{\tau}^{\alpha}}{\mathrm{d}\Gamma} \sum_{\beta=1}^{n} q^{\alpha\beta} \left|\dot{\gamma}^{\beta}\right| \tag{9}$$

with the extended Voce type hardening law of Tomé et al. [13]:

$$\bar{\tau}^{\alpha} = \tau_0 + (\tau_1 + \theta_1 \Gamma)\left[1 - \exp\left(-\frac{\Gamma\theta_0}{\tau_1}\right)\right]. \tag{10}$$

The quantities τ_0, τ_1, θ_0 and θ_1 are material-dependent parameters and are identical for all slip systems. While τ_0 and θ_0 describe the initial yield stress and initial hardening rate, the asymptotic hardening behaviour for large strains is characterised by τ_1 and θ_1. In Equations (9) and (10), Γ is the accumulated plastic shear strain over all slip systems n, which is expressed in terms of

$$\Gamma = \int_0^t \sum_{\alpha=1}^{n} |\dot{\gamma}^{\alpha}| \mathrm{d}t. \tag{11}$$

Interaction between two different slip systems α and β is incorporated by the interaction matrix $q^{\alpha\beta}$. The interaction matrix represents the latent hardening behaviour of a crystal. For self and coplanar slip systems, the entries of the interaction matrix are set to one. All other entries of the interaction matrix are specified by the parameter q.

The second crystal plasticity-based constitutive model utilises a physical-based hardening law. Therefore, a Taylor-type hardening model [14] is employed

$$\tau_f^{\alpha} = \tau_0 + \mu b \sqrt{\sum_{\beta} \tilde{q}^{\alpha\beta} \rho^{\beta}}, \tag{12}$$

where τ_0, μ and b are the lattice friction, the shear modulus, and the length of the Burgers vector, respectively. The variable ρ^{β} is the total dislocation density of a slip system β and is governed in accordance with Perdahcıoğlu et al. [15] as a linear ordinary differential equation

$$\dot{\rho}^{\alpha} = \frac{\dot{\gamma}^{\alpha}}{\gamma_s} (\rho_s - \rho^{\alpha}), \tag{13}$$

with ρ_s and γ_s denoting the saturation dislocation density and saturation shear rate, respectively. In the initial state, the total dislocation density ρ^{α} is defined by the initial dislocation density ρ_0. The variable $\tilde{q}^{\alpha\beta}$ in Equation (12) is the interaction matrix. In contrast to the first crystal plasticity-based constitutive model, this interaction matrix distinguishes six interaction types following Franciosi and Zaoui [16] and Kubin et al. [17]: self, coplanar, collinear, orthogonal, glissile and sessile.

3.2. Representative volume element

The representative volume element (RVE) for AA6014-T4 was generated by using the free software package Neper 3.5.2 [18]. It has a cubic shape with an edge length of 1.0 and contains 1000 grains. Each grain was assigned a crystallographic orientation, which was obtained from a reconstruction of an experimentally obtained orientation density function (ODF) using the MATLAB toolbox MTEX 5.7.0 [7]. The RVE was meshed by 40x40x40 linear hexahedral elements of type C3D8. As suggested by Schmidt [19], periodic boundary conditions were applied for constraining the RVE.

3.3. Crystal plasticity simulations

All crystal plasticity simulations were performed using the commercial finite element software Abaqus/Standard 2021. In that respect, two different kinds of crystal plasticity simulations were carried out: First, crystal plasticity simulations of the uniaxial tensile tests at 0° with respect to RD were performed to identify the crystal plasticity parameters describing the hardening behaviour for each crystal plasticity-based constitutive model. Thus, the hardening parameters were adjusted to match the experimental stress-strain curve. To this end, a reverse engineering approach using the commercial software LS-OPT 6.0 was used. Second, uniaxial tensile tests at 15°, 30°, 45°, 60°, 75° and 90° with respect to RD were simulated to predict the texture-induced plastic anisotropy. These simulations were performed on the base of a texture rotation, i.e. for each simulation, the RVE was loaded in RD with the texture rotated at the respective angle. As the grains of the studied RVE had an aspect ratio of 1.0, this approach is seen as reasonable.

4. Results

4.1. Experimental characterisation

The ODF in Figure 1 (a) shows a non-uniform distribution of crystallographic orientations. The maximum intensity amounts to 13 multiples of a random density (MRD). Areas with higher intensity are associated to the crystallographic orientation {001} <100> or rather the cube texture component.

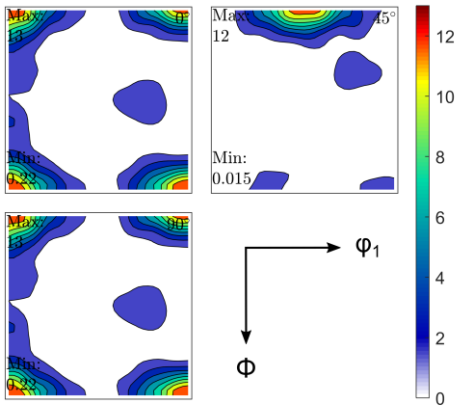

Figure 1. Orientation density function (ODF) of AA6014-T4 in the longitudinal cross-section shown as φ_2-sections from 0° to 90° in steps of 45° through the reduced Euler space.

The representative stress-strain curves of the uniaxial tensile tests at 0°, 15°, 30°, 45°, 60°, 75° and 90° with respect to RD in Figure 2 show a different hardening behaviour with respect to the angle considered. Therefore, AA6014-T4 exhibits a direction-dependent plastic material behaviour. As illustrated in Figure 5, the yield stresses were highest at 0° and lowest at 60° with respect to RD. The r-values were lowest at 45° with respect to RD.

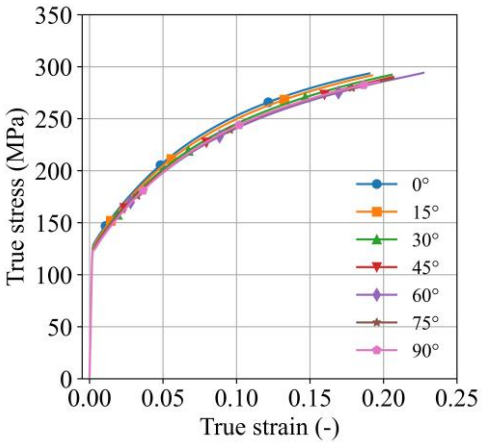

Figure 2. Stress-strain curves of uniaxial tensile tests at 0°, 15°, 30°, 45°, 60°, 75° and 90° with respect to the rolling direction (RD). One of three repetitions for each direction is illustrated.

4.2. Microstructure model

The RVE for AA6014-T4 as generated according to Section 3.2 is depicted in Figure 3 (a). The results of the parameter identification for the hardening parameters of both crystal plasticity-based constitutive models are illustrated in Figure 3 (b) in the form of the corresponding stress-strain curves in RD. Both formulations match the experimentally determined stress-strain curves in RD with good accuracy.

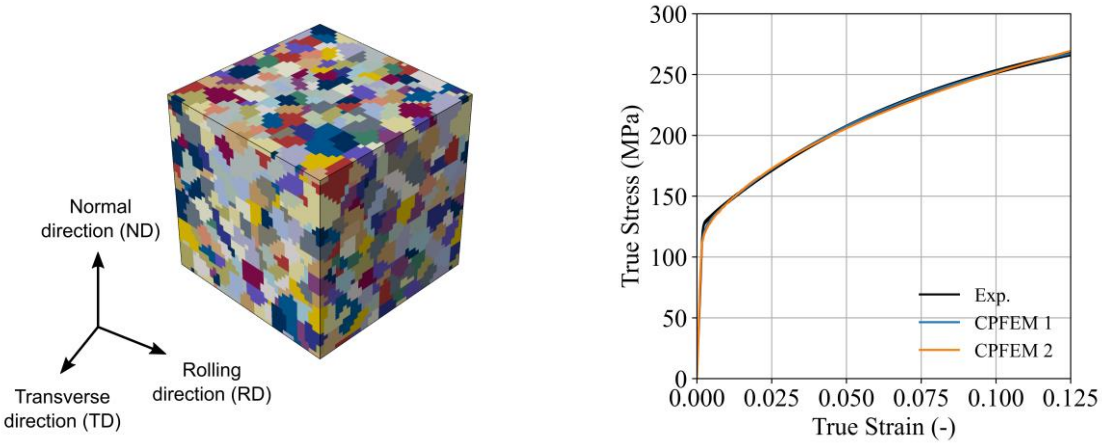

Figure 3. (a) Representative volume element (RVE) for AA6014-T4. Each set of equally coloured finite elements represents one grain of the microstructure. (b) Stress-strain curves as predicted by both crystal plasticity-based constitutive models in comparison with experimental data in RD.

All crystal plasticity parameters as identified by the reverse engineering approach as well as taken from the literature are summarised in Table 1 and Table 2 for both constitutive models. The parameters C_{11}, C_{12} and C_{44} are the elastic constants describing the fourth-order elasticity tensor for cubic crystals.

Table 1. Parameters as representative for AA6014-T4 utilised for the first crystal plasticity-based constitutive model (rate-dependent, phenomenological hardening law).

C_{11}[a] (MPa)	C_{12}[a] (MPa)	C_{44}[a] (MPa)	$\dot{\gamma}_0$[b] (-)	m[c] (-)	τ_0 (MPa)	τ_1 (MPa)	θ_0 (MPa)	θ_1 (MPa)	q[d] (-)
106750	60410	28340	0.001	0.0125	48.45	50.01	265.18	6.52	1.4

[a] Reference [20].
[b] Reference [4-5].
[c] Reference [6, 9].
[d] Reference [21].

Table 2. Parameters used for the second crystal plasticity-based constitutive model (rate-independent, physical-based hardening law) representing AA6014-T4.

C_{11}[a] (MPa)	C_{12}[a] (MPa)	C_{44}[a] (MPa)	b[b] (mm)	τ_0 (MPa)	ρ_0 (mm^{-2})	ρ_s (mm^{-2})	γ_s (-)	$\tilde{q}^{\alpha\beta}$[c] (-)
106750	60410	28340	2.86e-07	18.0	1.00e7	6.89e8	0.21	

[a] Reference [20].
[b] Reference [15, 22].
[c] Reference [17].

4.3. Prediction of plastic anisotropy

Results of the stress-strain curves at 15°, 30°, 45°, 60°, 75° and 90° with respect to RD as predicted by both crystal plasticity-based constitutive models are illustrated in Figure 4. Both formulations show similar results. With respect to the experimental results, there are differences depending on the direction of the uniaxial tensile test. In Figure 4 (a), the difference between the experimental and predicted stress-strain curves at 15° with respect to RD is rather small. For larger angles, this difference increases to its

maximum at 45°/60° with respect to RD before decreasing again. The best match between experimental and predicted stress-strain curves is given at 90° with respect to RD.

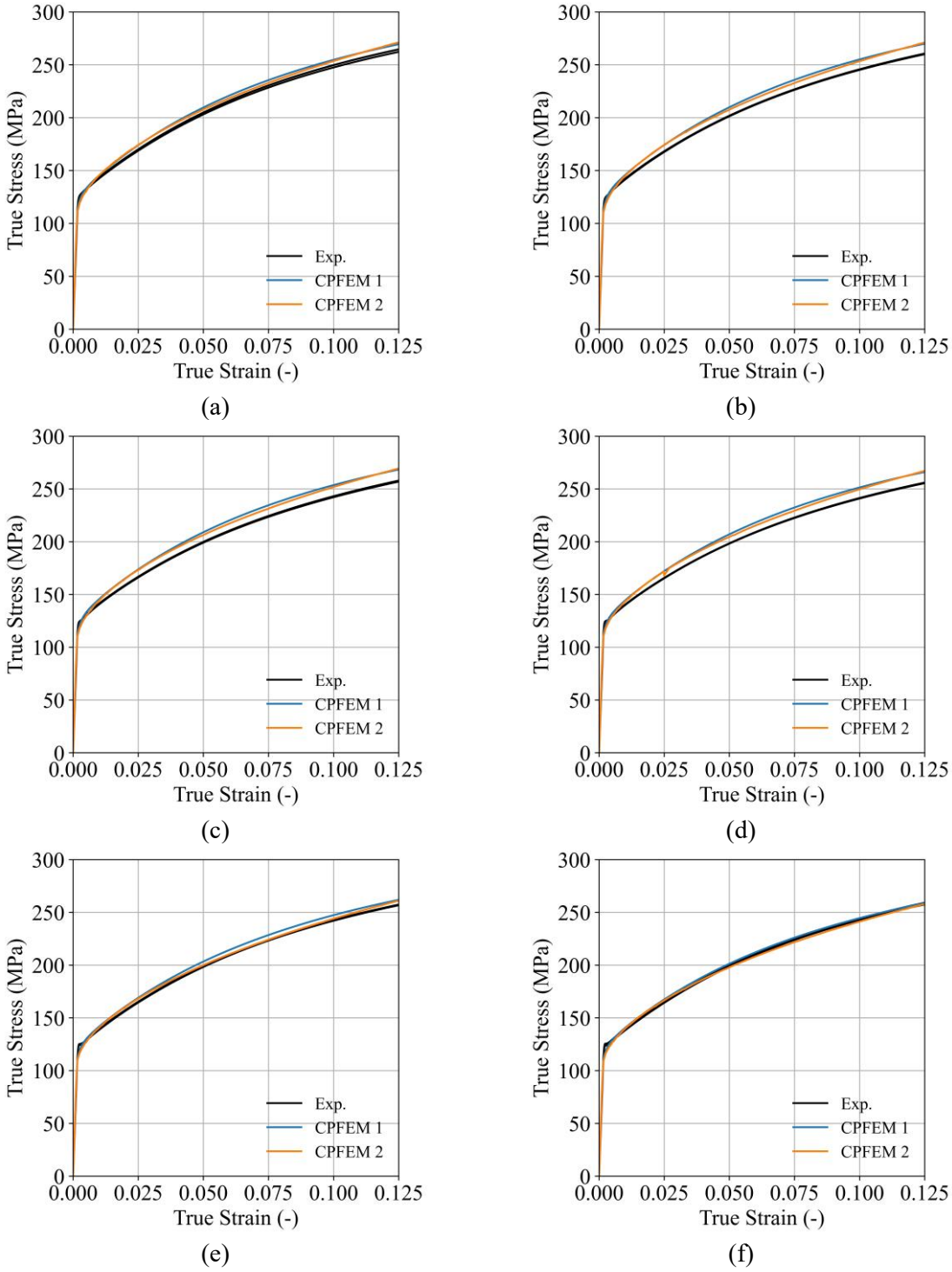

Figure 4. Stress-strain curves at (a) 15°, (b) 30°, (c) 45°, (d) 60°, (e) 75° and (f) 90° with respect to RD as predicted by both crystal plasticity-based models and compared with experimental data.

The normalised yield stresses were determined at a specific plastic work of 15.49 MPa, which corresponds to 0.08 true plastic strain and are shown in Figure 5 (a). In accordance with the results of the stress-strain curves in Figure 4, both crystal plasticity-based constitutive models are in good agreement. Again, there are differences with respect to the experiment. In the experiment, the normalised yield stress decreases from an angle at 0° to its minimum at 60° with respect to RD. In contrast to this, both crystal plasticity-based constitutive models predict a rather complementary behaviour with a maximum normalised stress at 30° with respect to RD. The results of the r-values in Figure 5 (b), which were analysed between 0.1 and 0.175 true plastic strain, demonstrate that both formulations can predict the experimental r-values with good accuracy.

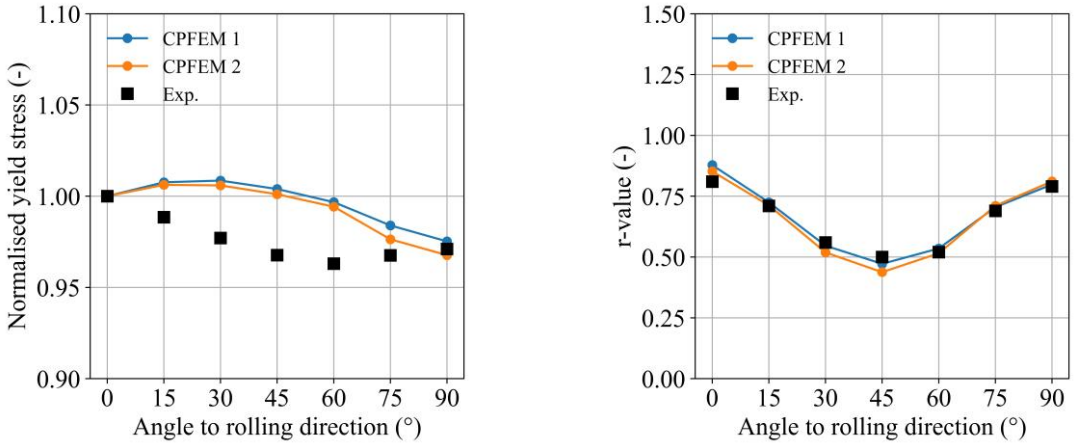

Figure 5. Experimental (a) normalised yield stresses and (b) r-values in comparison with results of both crystal plasticity-based constitutive models. Yield stresses were determined considering a specific plastic work of 15.49 MPa, which corresponds to a true plastic strain of 0.08, while r-values were analysed between 0.1 and 0.175 true plastic strain.

5. Discussion

The crystallographic and mechanical results in Section 4.1 indicate that the AA6014-T4 aluminium alloy exhibits a pronounced plastic anisotropy, which is in general agreement with data available in the literature. For example, Yoshida et al. [23] present uniaxial tensile test results at 0°, 15°, 30°, 45°, 60°, 75° and 90° with respect to RD for a non-specified AA6XXX aluminium alloy in T4 heat treatment condition. Both the normalised yield stresses and r-values reported are in good agreement with the experimental results generated in this study. In that respect, normalised yield stresses had their minimum at 60° with respect to RD, while the r-values were lowest at 45° with respect to RD. In addition, Kuwabara et al. [24] also performed uniaxial tensile test at 0°, 22.5°, 45°, 67.5° and 90° with respect to RD for aluminium sheets made out of AA6016-T4. Here, both normalised yield stresses as well as r-values were lowest at 45° with respect to RD.

With respect to the crystal plasticity simulations in Section 4.2 and Section 4.3, both crystal plasticity-based constitutive models are flexible enough to reproduce the experimental stress-strain curves in RD and show a rather similar behaviour. In addition, also the uniaxial stress-strain curves at 15°, 30°, 45°, 60°, 75° and 90° with respect to RD, the normalised yield stresses as well as r-values predicted by both crystal plasticity-based constitutive models are fairly similar. Overall, differences between both crystal plasticity-based constitutive models are rather small and seem to be negligible. With respect to the experimental data, the r-value is predicted with high accuracy for all directions. Also, the uniaxial stress-strain curve at 90° with respect to RD in Figure 4 (f) as well as the corresponding normalised yield stress in Figure 5 (a) are in good agreement with the experiment. In contrast to this,

there are slightly higher differences between the crystal plasticity simulations and the experimental yield stresses at 15°, 30°, 45°, 60° and 75° with respect to RD. The highest differences appear at 45° with respect to RD. Overall, these differences may still be reasonable, but they lead to a kind of opposite curve progression. Similar results for AA6XXX aluminium alloys in T4 heat treatment condition, i.e. crystal plasticity simulations predict a different curve progression for the normalised yield stress with respect to the experiment, were already reported by several authors. Examples are given in Yoshida et al. [23], Gawad et al. [25], Hama et al. [26], Pagenkopf [10], Hirsiger [27] and Habraken et al. [28].

A possible explanation for this difference between crystal plasticity simulations and experiments can also be found in the literature. Kuwabara et al. [24] utilised uniaxial tensile tests at 0°, 22.5°, 45°, 67.5° and 90° with respect to RD for an AA6016 aluminium alloy in T4 and O heat treatment conditions. While the normalised yield stress at 45° with respect to RD was lowest for the AA6016-T4 aluminium alloy, it was highest for AA6016-O. At the same time, the r-values for both aluminium alloys were nearly similar. According to Kuwabara et al. [24], the main difference between both aluminium alloys was the existence of GP-zones in the case of the T4 heat treatment condition. Thus, it was concluded that for AA6016-O the plastic anisotropy was controlled by crystallographic texture alone, whereas that for AA6016-T4 was governed by crystallographic texture and GP-zones. Also, Yoshida et al. [23] pointed out that the difference between experimental results and crystal plasticity simulations for a non-specified AA6XXX-T4 aluminium alloy may be caused by GP-zones or rather GP-zone related effects. Moreover, in the early 70s, Hosford and Zeisloft [29] already suggested that precipitates – GP-zones are an early stage of precipitation – in AA2XXX aluminium alloys can affect the texture-induced plastic anisotropy. Hence, there seems to be some evidence that the plastic anisotropy of the AA6014-T4 aluminium alloy studied is controlled by crystallographic texture as well as GP-zone/precipitate related effects. As both crystal plasticity-based constitutive models predict the plasticity anisotropy of AA6014-T4 aluminium alloy based on crystallographic texture alone, some differences with respect to experiments – specifically for the normalised yield stress at 45° with respect to RD – appear. In that respect, it is assumed that an extension of the crystal plasticity-based constitutive models regarding the effect of GP-zones/precipitates could improve the prediction accuracy of the crystal plasticity approach with respect to age-hardenable aluminium alloys.

6. Conclusions

In this study, two crystal plasticity-based constitutive models that differ with respect to the flow rule (rate-dependent/rate-independent) and hardening law (phenomenological/physical-based), among other aspects, were utilised to predict the texture-induced plastic anisotropy for an AA6014-T4 aluminium alloy. In summary, the following conclusions can be drawn from the present work:

- Both crystal plasticity-based constitutive models are suitable to predict the texture-induced plasticity anisotropy for an AA6014-T4 aluminium alloy. In particular, the r-values are predicted with high accuracy.
- Differences with respect to the prediction of the normalised yield stresses are observed in both crystal plasticity models. These differences are most likely caused by GP-zone/precipitate related effects that are not included in either crystal plasticity-based constitutive model yet.

Acknowledgement

The authors gratefully acknowledge funding from the Federal Ministry for Economic Affairs and Climate Action via the German Federation of Industrial Research Associations – AiF (Arbeitsgemeinschaft industrieller Forschungsvereinigungen e.V.) within the scope of the programme for Industrial Collective Research (Industrielle Gemeinschaftsforschung, IGF), grant numbers 19707 N and 21466 N. The authors would also like to thank Jürgen Timm from Novelis Switzerland SA for providing the AA6014-T4 aluminium sheets. A. Wessel would like to acknowledge the Fraunhofer-Gesellschaft for funding his 5-month research stay at the University of Twente via the Fraunhofer International Mobility (FIM) programme.

References

[1] Banabic D, Barlat F, Cazacu O and Kuwabara T 2010 *Int. J. Mater. Form.* **3** 165–89
[2] Banabic D, Barlat F, Cazacu O and Kuwabara T 2020 *Int. J. Mater. Form.* **13** 749–87
[3] Barlat F, Aretz H, Yoon J W, Karabin M E, Brem J C and Dick R E 2005 *Int. J. Plast.* **21** 1009–39
[4] Zhang K, Holmedal B, Hopperstad O S, Dumoulin S, Gawad J, Van Bael A and Van Houtte P 2015 *Int. J. Plast.* **66** 3–30
[5] Zhang H, Diehl M, Roters F and Raabe D 2016 *Int. J. Plast.* **80** 111–38
[6] Wessel A, Morand L, Butz A, Helm D and Volk W 2022 *Preprint* arXiv:2211.00090
[7] Bachmann F, Hielscher R and Schaeben H 2010 *Solid State Phenom.* **160** 63–8
[8] Field D P 1997 *Ultramicroscopy* **67** 1–9
[9] Kalidindi S R, Bronkhorst C A and Anand L 1992 *J. Mech. Phys. Solids* **40** 537–69
[10] Pagenkopf J 2018 *PhD Thesis* Fraunhofer Verlag, Stuttgart
[11] Aşık E E, Perdahcıoğlu E S and van den Boogaard T 2020 *Materials* **13** 1795
[12] Lebensohn R A, Tomé C N and CastaÑeda P P 2007 *Philos. Mag.* **87** 4287–322
[13] Tome C, Canova G R, Kocks U F, Christodoulou N and Jonas J J 1984 *Acta Metall.* **32** 1637–53
[14] Taylor G I 1934 *Proc. R. Soc. Lond. A* **145** 362–87
[15] Perdahcıoğlu E S, Soyarslan C, Aşık E, van den Boogaard T and Bargmann S 2018 *Materials* **11** 1425
[16] Franciosi P and Zaoui A 1982 *Acta Metall.* **30** 1627–37
[17] Kubin L, Devincre B and Hoc T 2008 *Acta Mater.* **56** 6040–9
[18] Quey R, Dawson P R and Barbe F 2011 *Comput. Methods Appl. Mech. Eng.* **200** 1729–45
[19] Schmidt I 2011 *Comput. Mech.* **48** 579–90
[20] Frederikse H P R 2014 *CRC Handbook of Chemistry and Physics* ed Hayne W M (Boca Raton: CRC Press)
[21] Kocks U F 1970 *Metall. Mater. Trans. B* **1** 1121–43
[22] Hansen N and Huang X 1998 *Acta Mater.* **46** 1827–36
[23] Yoshida K, Yamazaki Y and Nakanishi H 2021 *Metals* **11** 1979
[24] Kuwabara T, Mori T, Asano M, Hakoyama T and Barlat F 2017 *Int. J. Plast.* **23** 164–86
[25] Gawad J, Banabic D, Van Bael A, Comsa D S, Gologanu M, Eyckens P, Van Houtte P and Roose D 2015 *Int. J. Plast.* **75** 141–69
[26] Hama T, Yagi S, Tatsukawa K, Maeda Y, Maeda Y and Takuda H 2021 *Int. J. Plast.* **137** 102913
[27] Hirsiger S 2020 *PhD Thesis* ETH Zurich, Zurich
[28] Habraken A M, Aksen T A, Alves J L, Amaral R L, Betaieb E, Chandola N, Corallo L, Cruz D J, Duchêne L, Engel B, Esener E, Firat M, Frohn-Sörensen P, Galán-López J, Ghiabakloo H, Kestens L A I, Lian J, Lingam R, Liu W, Ma J, Menezes L F, Nguyen-Minh T, Miranda S S, Neto D M, Pereira A F G, Prates P A, Reuter J, Revil-Baudard B, Rojas-Ulloa C, Sener B, Shen F, Van Bael A, Verleysen P, Barlat F, Cazacu O, Kuwabara T, Lopes A, Oliveira M C, Santos A D and Vincze G 2022 *Int. J. Mater. Form.* **15** 61
[29] Hosford W F and Zeisloft R H 1972 *Metall. Mater. Trans. B* **3** 113–21